FINAL REPORT

FEASABILITY STUDY ON HAND-HELD ULTRA-HIGH DATA DENSITY NANOMETROLOGY AND NANOWRITING SYSTEM

Project: 25066QR

Date Prepared: January 15, 2008

SUMMARY:

The goal of this project was to demonstrate feasibility of developing a hand-held system for nanometrology and nanowriting. In the final phase of the work, we developed cantilever probe arrays, which form the essential core of the nanometrology system. The following describes the design, fabrication, characterization, and use of these probe arrays for nanometrology. In doing so, we have completed all of the originally proposed work.

Improved All-Silicon Microcantilever Heaters with Integrated Piezoresistive Sensing

This technical document presents design, fabrication, and characterization of improved all-silicon microcantilever heaters with integrated piezoresistive sensing. The fabricated microcantilever heaters with piezoresistors are made solely from single crystal silicon with selective doping. Detailed characterization was performed to test the device electrical, thermal, and mechanical properties. The performance of and crosstalk between heater and piezoresistor elements was thoroughly tested. The resistive heater can reach temperature > 600 °C, and its temperature coefficient of electrical resistance was (2.01 ± 0.04) × 10^{-3} Ω/Ω-°C. When biased at 2 V in a Wheatstone bridge, the deflection sensitivity of the piezoresistor was (4.25 ± 0.05) × 10^{-4} V/V-μm and remarkably, the heater circuit had a measureable deflection sensitivity of (7.9 ± 0.5) × 10^{-5} V/V-μm. Both the piezoresistor and the resistive heater were interfaced with a commercial atomic force microscope (AFM) system to measure their sensitivities during topography imaging. The sensitivity of thermal reading was much greater than that of piezoresistive reading. Noise-limited resolution of thermal reading was better than 0.46 ± 0.03 nm/$\sqrt{\text{Hz}}$ and piezoresistive reading was better than 3.4 ± 0.4 nm/$\sqrt{\text{Hz}}$. This is the first experimental comparison between thermal and piezoresistive topographic sensing both of which can replace optical lever sensing. Four cantilevers in an array demonstrated parallel topographic sensing with both the heater and the piezoresistor.

I. INTRODUCTION

Microcantilevers have shown their versatility in various applications ranging from scanning probe microscopy (SPM) to bio/chemical sensing. Single microcantilevers are capable of sub-nanometer topographic resolution in SPM [1] and femtogram adsorption/desorption detection in bio/chemical sensing [2]. A common requirement in microcantilever applications is array parallelization to increase throughput or to test many analytes simultaneously. Array operation may also offer differential measurements that could cancel unwanted measurement artifacts.

Microcantilever probe arrays have been used in data storage [3]–[7], nanolithography [8], [9], parallel imaging [10] and force spectroscopy in life science applications [11]. Arrays having up to 64 × 64 microcantilevers with integrated heaters have been used to demonstrate probe based data storage [12]. Each cantilever enables writing, reading, and erasing of nanoscale indents on soft polymeric media [13]. A 100 × 100 array of thermo-piezoelectric microcantilevers has been reported with further improved data bit density [14]. A multifunctional microcantilever probe array has been developed for nanoscale patterning and imaging using dip-pen nanolithography (DPN) and scanning probe contact printing [9]. A two dimensional array having 55,000 cantilevers in 1 cm^2 was fabricated to achieve extremely large area DPN [15]. This is the highest density and largest number of cantilevers ever reported. A 4 × 4 array of piezoresistive microcantilever probes was specifically designed and fabricated to image biological cells in a buffer solution and to perform force spectroscopy measurements on cells [11].

Another application of microcantilever arrays is bio/chemical sensing where physiorption or chemiorption processes are transduced into mechanical responses [16]. In contrast to microcantilever probe arrays for imaging, these microcantilever arrays often operate far away from any substrate and do not require a tip. A 1 × 8 array of microcantilevers with selective coatings has been applied as an artificial nose to recognize and characterize alcohol vapors either in a static mode [17] or in a dynamic mode [18]. Besides gas sensing, the same platform was introduced to investigate DNA hybridization [16], antibody-antigen interaction [19], [20], and two different DNA-binding proteins [21]. Recently, a 2D multiplexed array having 480 SiN/Au microcantilevers was fabricated to detect thermally induced phase transitions and stability of DNA [22].

Without regard to application, a major issue for the cantilever array operation is deflection sensing of each individual cantilever. For small arrays, optical sensing such as vertical cavity surface emitting lasers (VCSELs) can be used [17], [18], [21]. However, having a large number of microcantilevers in the array requires integrated deflection sensing schemes, such as piezoelectric sensing [14], piezoresistive sensing [23], and capacitive sensing [24]. Among them, piezoresistive sensing has been widely used mainly because of the high sensitivity and ease of fabrication and implementation. Piezoresistive sensing has been shown to be very sensitive with sub-nm minimum detectable deflection [25] and can be used in both static and dynamic modes for bio/chemical sensing.

A thermal element fabricated into the cantilever permits detection of topographical features in data storage [26]. The thermal detection mechanism has been thoroughly investigated in theoretical studies [27]–[29], and has been used for quantitative detection of nanometer-scale displacements [30] and for quantitative mapping of nanotopographical features [31], [32]. It has been suggested that the thermal sensing mechanism has a sensitivity that far exceeds that of piezoresistive sensing [27], [31]. However no paper has made a direct comparison the thermal and piezoresistive sensing mechanisms. The most compelling experiment that could be made would be using a cantilever having both piezoresistor and thermal elements. Microcantilevers having both a resistive micro heater and a piezoresistor have been fabricated for data storage [3], [33] as well as calorimetry and mass detection [34]. These previous publications focused on cantilever fabrication and operation, but did not focus on detailed characterization of the cantilever heater and piezoresistor elements. From these papers, it is not possible to support or refute claims about the relative sensitivity of thermal vs. piezoresistive sensing. The lack of comprehensive characterization limits the development of similar cantilevers.

Microcantilevers having both heaters and piezoresistive sensors would be useful in a number of applications. One example is thermal nano-manufacturing [35], [36] where the tip heating would perform writing but piezoresistive topography sensing would be preferred in the presence of a thermally-reactive substrate. A second example is topography sensing where cantilever heating could be used to perform local materials synthesis [37], chemical reaction [38], or to clean the tip [39], [40]. Finally, such a cantilever could be used to sense temperature sensitive biochemical binding events [22], [41].

This paper describes design, fabrication, and characterization of a small array of microcantilever heaters with integrated piezoresistors. The heater and piezoresistor devices are thoroughly characterized during individual and simultaneous operation. The paper aims to thoroughly understand the links between cantilever design, fabrication, and performance, and to measure the relative performance of the heater and piezoresistive elements.

II. DESIGN, SIMULATION, AND FABRICATION

A. Microcantilever Array Design

The design of the cantilever array is based on the silicon microcantilever heater reported in [42]. Fig. 1 shows the cantilever design, in which each cantilever has four legs. The two outer legs are highly-doped to act as electrical leads to the resistive heater near the cantilever free end and the two inner legs will be used to define piezoresistors. Previous microcantilevers having both resistive heaters and piezoresistive sensors [3], [33] employed metal traces for carrying current. These metal traces placed limits on the device performance, including thermomechanical bending, temperature limits, and electromigration when the leads carried high current density. Here we use doped silicon for the current-carrying traces as well as for the active heater and piezoresistive elements. By placing metal to doped silicon contacts far away from the hot spot, temperature at contacts can be greatly reduced. For a given current density (J), when temperature (T) at silicon to aluminum contacts is lowered from 400 K to 300 K, mean time to failure (MTF or MTTF) given by [43]

$$MTF \propto \frac{1}{J^2}\exp\left(\frac{E_A}{k_B T}\right) \tag{1}$$

can be improved by about a factor of 3,300 where E_A is the activation energy of 0.84 eV for well-ordered and large-grained aluminum films [43] and k_B is the Boltzmann constant. There are additional advantages using doped silicon current traces over metal traces on cantilevers. Since melting point of silicon is much higher than that of frequently used metal as interconnects – for example, melting points of silicon and aluminum are 1412 °C and 660 °C, respectively.–, the temperature range for device operation can be significantly extended beyond 1000 °C. Therefore, higher current density can be accommodated at temperatures higher than melting point of the metal without electromigration failure. While the packaged cantilever would not be able to operate in environments where the temperature exceeded the limits of the package or the metal-semiconductor junction, the local maximum temperature in the cantilever heater can far exceed these limits. By moving the metal-semiconductor junction away from the cantilever heater, the cantilever heater can reach higher temperatures than in some previous designs. Moreover, metals have far different coefficient of thermal expansion (CTE) than silicon, it would be better not to use metals on cantilevers unless vertical bimorph actuation is required. For cantilevers using high-doped silicon as current traces, no observable thermomechanical bending has been reported since CTE of the doped silicon layer is similar to that of intrinsic silicon. However, thermal bimorph bending (d) of cantilevers with metal current traces given by [44]

$$d = \frac{3E_1E_2t_1t_2\left(t_1+t_2\right)l^2\left(\alpha_1-\alpha_2\right)\Delta T}{\left(E_1t_1^2\right)^2+\left(E_2t_2^2\right)^2+2E_1E_2t_1t_2\left(2t_1^2+3t_1t_2+2t_2^2\right)} \tag{2}$$

could range from a few μm to several tens of μm for typical cantilever dimension and temperature range of our interest, where t is layer thickness, l is cantilever length, E is elastic modulus, α is CTE, ΔT is temperature change, and subscripts 1 and 2 denote metal current trace and silicon device layer.

The U-shaped cantilever is used to achieve thermal isolation between the heater and the piezoresistor. In addition, U-shaped design cantilevers have shown better performance in piezoresistive sensing than rectangular ones [45]. The length of the inner legs, which is equivalent to that of the piezoresistor, is chosen to be about 0.4 of the overall cantilever length, which is a design criterion that optimizes both resolution and sensitivity [46]. The extender location is the preferred site for the piezoresistors in order to maximize deflection sensitivity.

Fig. 1 shows the design of the microcantilever, the different dopant species and regions for the heater and the piezoresistor, and dimensions for an individual cantilever. For doping the active silicon elements, phosphorus was chosen for the heater and the two outer legs because phosphorus has a lower resistivity than boron at a given doping concentration [47]. However, boron was chosen for the piezoresistor to construct *p-n* junctions between the inner and the outer legs thus prevent electrical crosstalk between the heater and the piezoresistor. Similar approaches to minimize crosstalk have been reported using *p-n* junctions in two different directional piezoresistive elements [48] and Schottky diodes between each cantilevers in a cantilever array [5], [7]. In addition, boron has a higher piezoresistive coefficient than phosphorus in the <110> crystal direction.

B. Mechanical and Electrical Simulation

Because of the complex cantilever geometry, finite element simulation was required to understand resonance frequency and spring constant. The finite element simulations allowed us to find appropriate analytical expressions of cantilever mechanical properties, which in turn allowed detailed design. To this end, static and eigenfrequency analyses in FEMLAB 3.1 (a finite element package, COMSOL Inc.) were employed. Due to the complex cantilever geometry, the simulated resonance frequency and spring constant were not directly proportional to cantilever thickness (t) and its third power, respectively. However, plane view dimensions such as width and length are fixed, simulated resonance frequency (f_0) and spring constant (k) can be fitted with appropriate polynomials of cantilever thickness.

$$f_0(t)\ [\text{kHz}] = 0.534 + 25.688t \tag{3}$$

$$k(t)\ [\text{N/m}] = -3.306 + 3.299t - 1.088t^2 + 0.204t^3 \tag{4}$$

where thickness unit is μm and thickness ranges from 0.5 to 3.5 μm. The cantilever thickness can thus be easily estimated from (3) or (4) once either the resonance frequency or the spring constant is measured. To relate resonance frequency with spring constant, the microcantilever structure can be modeled as a simple harmonic oscillator, although the cantilever mass should be corrected. This corrected mass is often referred to as effective mass (m_{eff}). The resonance frequency of the microcantilever is

$$f_0 = \frac{1}{2\pi}\sqrt{\frac{k}{m_{\text{eff}}}} = \frac{1}{2\pi}\sqrt{\frac{k}{C_{\text{m}}m}} \tag{5}$$

where m is the total mass and C_{m} is the correction factor. For example, the effective mass of a simple rectangular cantilever is 24% of the total mass. For the present cantilever, finite element simulations provide a correction factor of 0.148. These mechanical modeling results facilitate cantilever calibration.

The microcantilever arrays are made of doped single crystalline silicon. In order to design doped silicon devices, it is important to estimate the resistivity and device resistance after implantation and diffusion since thermophysical properties and heating characteristics of doped silicon devices strongly depend upon local resistivity. Furthermore, the performance of a piezoresistor depends upon both doping concentration and the distribution of dopants in the silicon layer [46], [49]. To introduce dopants into the device layer in the microcantilever array, ion implantation was chosen over diffusion since implantation is a low temperature process and offers more precise doping control. Since single crystalline silicon is the starting material, the introduction of a 7° wafer tilt angle during implantation prevents ion channeling such that the Gaussian distribution well describes doping profiles after implantation.

The implant energy, dose, and subsequent diffusion time were selected using a one-dimensional dopant diffusion simulator. The developed simulator incorporates both intrinsic and extrinsic diffusion to solve a diffusion equation described by Fick's first and second laws numerically. When the doping concentration is less than the intrinsic carrier concentration at diffusion temperature, diffusivity is independent of local doping concentration (*intrinsic diffusion*). However, diffusivity becomes concentration-dependent when the doping concentration exceeds the intrinsic carrier concentration (*extrinsic diffusion*). After local doping concentration was obtained from the diffusion simulation, the local electrical resistivity was calculated by $\rho = 1/\left[q\left(\mu_n N + \mu_p P\right)\right]$ where q is the electron charge and μ_n and μ_p are electron and hole mobility, respectively. Bulk mobility models for electron and hole were adopted from [50]. Finally, calculated local resistivity was used to calculate device resistance per unit length using a parallel resistor network [51] and the actual device resistance was obtained considering the finalized geometry of the device. A commercial dopant diffusion simulator (SUPREME3) was used to check the results, and there was very close agreement between our simulation and the predictions of the commercial software. Fig. 2 shows predicted doping concentration and resistivity of low-doped phosphorus, high-doped phosphorus, and medium-doped boron that are obtained from the developed simulation. Simulated device resistances are compared with measurements in a following section.

C. Microcantilever Array Fabrication

Fig. 3 shows the seven major fabrication steps to make the microcantilever array. The fabrication process started with an *n*-type silicon-on-insulator (SOI) wafer of orientation <100>, where the silicon device layer was 5 μm, the buried oxide layer was 1 μm, and the silicon handle layer was 500 μm. Background doping in the device layer was 1×10^{15} cm^{-3} with a resistivity of approximately 4 Ω-cm. The first step was to define a probe tip via dry isotropic silicon etch followed by oxidation sharpening. Then, photolithography patterned negative photoresist (Futurrex NR7-1500) to define the cantilever structures. A Bosch process using inductively coupled plasma (ICP) etched the patterned window all the way through the device layer until the buried oxide layer was fully exposed. After the probe tip and beam structures were defined in the device layer, three implantation steps were performed with hard-baked positive photoresist (Shipley 1827) as a mask for ion implantation. The first implantation doped the heater region near the free end with 2.51×10^{13} cm^{-2} of phosphorous at 200 keV. A post diffusion step was performed for 6 hrs at 1000 °C in the furnace to distribute the implanted dopant uniformly. The second implantation step doped the two outer legs with 2.51×10^{16} cm^{-2} of phosphorous at 200 keV and a post diffusion step was performed for 2 hrs at 1000 °C in the furnace. The two implantations finalized the *n*-type resistive heater. The final implantation defined the piezoresistor in the two inner legs with 2×10^{14} cm^{-2} of boron at 30 keV. The implanted boron was annealed for 20 min at 1000 °C in a rapid thermal processing chamber. After metallization and lift-off to define aluminum-doped silicon contacts, the backside of the handle wafer was etched using ICP until the buried oxide layer was exposed. The cantilever arrays were finally released by a 15 s dip in 49% hydrofluoric acid.

Arrays were batch-fabricated with 90% yield so that 200 fully functional arrays were extracted from a 100 mm wafer. Figs. 4(a) and (b) show scanning electron micrographs (SEMs) of the fabricated microcantilever array. The inset in Fig. 4(a) shows the probe tip near the low-doped resistive heater. Fig. 4(c) shows a custom printed circuit board (PCB) to mount the array chip and a flexible ribbon cable for electrical connection to power supply and front end of data acquisition.

III. CHARACTERIZATION

A. Single Cantilever Characterization

After the array fabrication, individual microcantilever characterization was performed following the characterization techniques described in [42]. For the electrical testing, the cantilever was configured in series with precision 1 and 10 $k\Omega$ power resistors for heater and piezoresistor, respectively. The cantilever was excited with dc voltage to investigate steady state responses. Fig. 5(a) shows the dc response of the heater defined near the free end and connected through the two outer highly conductive legs, which is typical of heated cantilevers [5], [42], [52], [53]. The critical power, P_{crit}, at which the temperature coefficient of resistance (TCR) changes from positive to negative was 18 mW and the corresponding critical temperature, T_{crit}, was 560 °C. The TCR changes sign due to thermal runaway in the doped silicon, which is well understood for microcantilever heaters [42]. Fig. 5(b) shows the dc response of the *p*-type piezoresistor defined in the two inner legs. Temperature data were collected using Raman spectroscopy as explained in detail in [42], [54], [55]. Figs. 5(c) and (d) show the comparison of the normalized electrical resistances of the heater and the piezoresistor as functions of power dissipation and maximum temperature in each doped resistor, respectively. From Fig. 5(d), the TCR of the doped resistor was obtained. The TCR of the heater was $(2.01 \pm 0.04) \times 10^{-3}$ Ω/Ω-°C and the TCR of the piezoresistor was $(8.3 \pm 0.4) \times 10^{-4}$ Ω/Ω-°C. The higher TCR in the heater is mainly due to its lower doping level, but also due to the different dopant type.

To test electrical crosstalk between the heater and the piezoresistor, two legs on the left or right were connected to a dc power (see inset in Fig. 6) and diode characteristics of the *p-n* junction were measured. Fig. 6 shows measured I-V characteristics of the *p-n* junction between one leg for the heater and one leg for the piezoresistor for both forward and reverse bias. The on voltage (forward voltage drop) around 0.6 V is appropriate for a silicon *p-n* junction diode [56]. The breakdown voltage is around -10.5 V. However, there also exist Schottky barrier diodes and contact resistances between metal and doped silicon so that the measured I-V characteristics can not be simply expressed with an equivalent circuit of a *p-n* junction diode. When it is inevitable to have a voltage potential between two adjacent legs making a *p-n* junction (cross voltage potential), the bias direction needs to be determined carefully to minimize electrical crosstalk. Possible current leakages depend on the bias direction with same cross voltage potentials. For example, the current flow could be only 3 μA for reverse bias or as high as 0.698 mA for forward bias with 3 V cross potential.

To test thermal crosstalk and to visualize the temperature field in the cantilever, the temperature distribution both in the heater and in the piezoresistor was investigated using IR microscopy (Infrascope II, Quantum Focus Instruments). Prior to temperature measurements, local emmissivity for each pixel was obtained from reference radiance calibration. Then, fifty measurements were made at about 1 Hz and averaged. A more detailed description of the experimental procedure can be found in [57]. Fig. 7 shows temperature distributions when the heater and the piezoresistor were heated to 5 mW, either individually or simultaneously. The apparent asymmetric temperature distribution and hot spot offsetting from the free end are due to intrinsic artifacts and spatial resolution limits in the IR setup. The Raman measurements provided accurate local temperature measurements. The additional 5 mW in the piezoresistor elevates the average temperature in the conductive legs, but does not affect the maximum heater temperature since the heat generated in the piezoresistor is mostly dissipated into the adjacent air and the silicon handle. Only a small portion of this heat is directed to the free end of the cantilever. Despite the average temperature rise in the conductive legs, piezoresistive heating

effect is negligible considering its contribution to the overall heater resistance and much lower TCR than the resistive heater. For practical uses, the power dissipation in the piezoresistor will be less than 1 mW so that the heater temperature can be maintained regardless of the piezoresistor operation. However, temperature rise in the piezoresistor due to the heater operation might not be negligible since high temperature heater operation is often required. For such cases, switching operation between two elements is recommended. This crosstalk could be further suppressed by integrating a dielectric material between the two elements, which would provide increased thermal and electrical resistance. However the presence of the dielectric would probably induce thermomechanical bending in the cantilever.

The most important characteristic for the piezoresistive element is deflection sensitivity. To test the piezoresistor, a precision 3 axis microstage having 50 nm minimum increments was incorporated with a tungsten needle probe, a 3 axis coarse manual stage, and a charge-coupled device (CCD) camera. The setup was similar to that used in [58]. While the needle probe deflected the microcantilever tip, resistance changes were recorded. The cantilever was mounted in a Wheatstone bridge. Since light intensity can change the resistance of the doped silicon, the intensity of the coaxial light source for the CCD was fixed during deflection sensitivity measurements.

The deflection sensitivities of the heater and the piezoresistor were measured, first under independent operation and then together. Fig. 8(a) shows the voltage change in the piezoresistor as a function of the tip deflection where the applied voltage to the Wheatstone bridge was 2 V. When the piezoresistor was operated alone, its deflection sensitivity was $(4.25 \pm 0.05) \times 10^{-4}$ V/V-μm, which corresponded to a $\Delta R/R$-μm sensitivity of $(17.0 \pm 0.2) \times 10^{-4}$. Since both the mechanical properties of the microcantilever and the piezoresistivity of the doped silicon can be modulated upon heating, it is important to understand the piezoresistor deflection sensitivity while the resistive heater is powered. Figs. 8(a) and (b) show that the deflection sensitivity decreases as power dissipation in the heater increases. When the piezoresistor temperature increases due to the power input in the heater, the piezoresistive coefficients decrease [59]. In addition, the elastic modulus of the silicon decreases upon heating so that the cantilever becomes softer. For a given deflection, the soft cantilever will experience less stress change than the stiff cantilever. These two effects are combined and decrease the deflection sensitivity of the piezoresistor upon heating. Heating affects not only the deflection sensitivity but also the offset in the voltage output from the bridge. To measure the voltage offset upon heating, the tungsten needle probe was brought into contact with the microcantilever probe tip and the Wheatstone bridge was tuned to give zero output voltage. Then, the resistive heater was heated with a certain power and the voltage output from the bridge was measured without deflection. Fig. 8(c) shows that the voltage offset from the initially balanced Wheatstone bridge linearly increases with power dissipation in the heater.

It is typically assumed that microcantilever heaters having high-doped legs will have negligible piezoresistive effect [42], since high-doped silicon has very low piezoresistivity [59]. In addition to low piezoresistivity in the high-doped legs, resistance in the legs which is 10 % of the overall cantilever resistance at most [60], further suppresses the cantilever resistance change attributed to the cantilever deflection. If the cantilever leg resistance is negligible, the cantilever electrical resistance is dominated by temperature modulation. Little if any effort has been made to measure deflection sensitivity of microcantilever heaters while their vertical displacement sensitivity has been well thoroughly investigated [29], [30]. The cantilever heater was configured in a second Wheatstone bridge set to 2 V and, the voltage output was measured and it

is shown in Fig. 8(d). The deflection sensitivity of the heater obtained from the linear fit was $(7.9 \pm 0.5) \times 10^{-5}$ V/V-μm, which corresponded to a $\Delta R/R$-μm sensitivity of $(3.2 \pm 0.2) \times 10^{-4}$.

Table I summarizes basic characterization results and includes simulated electrical resistances which show good agreement with the measurement. Characterized mechanical properties such as spring constant, resonance frequency, and quality factor are also included in Table I.

B. Cantilever Topography Reading

It is expected that the piezoresistor deflection sensitivity will be the same for either a point deflection measurement or topography reading, since the piezoresistor is a strain sensor. The thermal signal from the cantilever heater can be used for topography mapping by measuring thermal conductance between the cantilever to the substrate [31], [32]. It is expected that the heater topography sensitivity will be much different from the heater deflection sensitivity. To test the topography sensitivity of the piezoresistor and the heater, the cantilever array was mounted in a commercial AFM system (MFP-3D, Asylum research) to scan a calibration grating. The silicon grating had 200 nm mesas that were evenly spaced. The two Wheatstone bridges were interfaced with data acquisition inputs into the AFM controller.

When the cantilever deflected against the calibration grating, the resistance of the piezoresistor changes and this unbalanced the Wheatstone bridge configured for the piezoresistor (*piezoresistive reading*). When the gap distance between the cantilever heater and the substrate changed, the thermal resistance from the cantilever to the substrate was modulated. This modulation changed the cantilever temperature which was transduced into the voltage signal from the Wheatstone bridge configured for the heater (*thermal reading*). This thermal reading concept originates from thermomechanical data storage research [26] and detailed demonstrations in contact mode [31] and tapping mode [32] have recently been reported. Theoretical and experimental studies have been published to compare the sensitivity of piezoresistive and thermal sensing. However, previous work employed two similarly sized cantilevers that have either resistive heaters or piezoresistors in simulations [27] or experimented only on thermal reading, and then compared its sensitivity to previously reported sensitivities for piezoresistive reading [31]. The most relevant comparison could be performed on the same cantilever which enables both thermal and piezoresistive reading but this has not been reported.

While the cantilever scanned the grating with the proportional-integral feedback loop turned off (*constant height mode or deflection mode*), either the piezoresistive reading or the thermal reading was recorded. Fig. 9 shows the piezoresistive reading and the thermal reading when the bias voltage to each Wheatstone bridge were 4 V and 5 V. The scan area was 30×30 μm^2, the scan rate was 1 Hz (1 scan line/sec), and each frame had an image resolution of 256×256 pixels. When one doped resistor, either the piezoresistor or the heater, was powered, the other one was not used. The images on the left show filtered piezoresistive readings with 42.3 Hz cut-off frequency and 20 dB output gain. The images on the right show unfiltered thermal readings. When the same bias voltages were used, the signal was too low to be measured with our electronics and so the piezoresistor readings were filtered and amplified, although the cut-off frequency of 42.3 Hz could distort the signals. In contrast, thermal readings were sensitive enough not to require filtering. Piezoresistive signals linearly increased with the bias voltage to the Wheatstone bridge and the measured topography sensitivity was approximately $(2.57 \pm 0.05) \times 10^{-7}$ V/V-nm when the bias voltage was less than 6 V. The thermal topography sensing was much more sensitive than the piezoresistive sensing, as expected from previous publications [27],

[31]. Thermal reading sensitivity ranged from $(1.00 \pm 0.05) \times 10^{-6}$ to $(5.89 \pm 0.04) \times 10^{-6}$ V/V-nm when the bias voltage changed from 3 to 6 V.

After the independent operation of each doped resistor was performed, both the piezoresistor and the heater were powered simultaneously when the cantilever scanned the calibration grating. Fig. 10 shows the piezoresistive reading and the thermal reading when the bias voltage to each Wheatstone bridge were 4 V and 5 V. The other scanning parameters remained unchanged. Again, the images on the left show filtered piezoresistive readings and the images on the right show unfiltered thermal readings. Thermal readings were similar and comparable to the results from the independent operation since the additional heating from the piezoresistor would not affect the resistive heater temperature. However, the piezoresistive readings were significantly different to the results in independent operation (Fig. 9). Their signals showed steep increase with the bias voltage so that the topography sensitivity was not constant any more. Moreover, the sensitivity increased rather than decreased with the bias voltage. This is counter-intuitive since Fig. 8 confirmed that the deflection sensitivity of the piezoresistor decreases as power dissipation in the heater increases. As mentioned above, the laser optical feedback was turned off during the scanning so that the cantilever deflection or contact force could not be controlled. Thus, the gap distance between the cantilever legs and the substrate may have varied significantly. When the power dissipation in the heater is sufficiently high enough to increase the temperature of the piezoresistor, the temperature change in the piezoresistor due to the gap distance modulation could be significant. The temperature change in the piezoresistor unbalances the Wheatstone bridge and signal due to the temperature modulation exceeds signal due to mechanical deflection. This is the most probable explanation for the enhanced piezoresistive readings when both the piezoresistor and the heater are powered. To confirm this, one cantilever in the array scanned the grating in a constant force mode with optical feedback while both the piezoresistor and the heater were powered. Output from the piezoresistor was similar magnitude to results in Fig. 10 and increased with the bias voltage. Since there was no additional strain in the piezoresistor after the cantilever engaged to the grating in a constant force mode, output from the piezoresistor was only due to its temperature modulation via air gap change during scanning.

Fig. 11 summarizes the topography sensitivity results for comparison between the piezoresistive reading and the thermal reading for both independent and combined operation. Even though the piezoresistor was designed to transduce mechanical strain into a measurable electrical signal, it could be better to use it as a thermal displacement sensor when the temperature of the piezoresistor is sufficiently high. Interestingly, the topography sensitivity of the piezoresistive reading might exceed that of the thermal reading at bias voltages above 6 V. Since we have fully characterized the heater and the piezoresistor for both independent and combined operation, both elements can be used simultaneously even thought this is not our primary interest. Temperature rise in the piezoresistors during heater operation can not be circumvented so that higher doping concentration for piezoresistors is recommended to reduce temperature dependence of piezoresistive coefficients for applications requiring simultaneous heater and piezoresistor operation. However, higher doping results in reduced piezoresistive coefficients.

Noise measurements were performed for both the piezoresistor and the heater using a low noise pre-amplifier (SR560, Stanford research systems) and a spectrum analyzer (SR770, Stanford research systems). Using measured noise spectra and topographic sensitivities, noise-limited resolutions were directly calculated (Resolution = Noise / Sensitivity). Table II

summarizes sensitivity, noise, and resolution for tested bias voltages. Thermal reading is superior to piezoresistive reading in terms of minimum detectable topographic change. With 3V bias to each Wheatstone bridge, noise-limited resolutions of thermal reading and piezoresistive reading were 0.46 ± 0.03 and $3.4 \pm 0.4\,\mathrm{nm}/\sqrt{\mathrm{Hz}}$, respectively. Resolution is improved as the bias voltage increases since sensitivity enhancements far exceed noise increase for the voltages tested. It is expected that resolution would be constant or reduced at higher bias voltages. The comparison is not necessarily a fair one due to their differences in sensing mechanism, size, resistance, and power consumption. Nevertheless, thermal reading senses the change in displacement but piezoresistive reading senses the change in cantilever deflection. Thus, thermal reading is applicable without contact to the substrate while piezoresistive reading is only possible with contact to the substrate.

C. Array Characterization

Since all cantilevers in an array chip were fabricated adjacent to each other, their dimensions including the cantilever thickness were more or less identical. Local variations during fabrication was not likely to exist within the areas of one array. The most relevant array characterization would be to scan the calibration grating using four cantilevers at the same time.

Fig. 12 shows the topography based on scans performed with optical reading, piezoresistive reading and thermal reading for four cantilevers in a single array chip. Four cantilevers were operated simultaneously but either the piezoresistor or the heater in a cantilever was powered at a time. The bias voltage was fixed at 4 V for both Wheatstone bridges. Before the array chip was attached and wire-bonded to the custom PCB, it was mounted on the dedicated cantilever holder in the commercial AFM. This enabled topography scans employing a laser and a photodiode. The images on the first row show the topography data from the four cantilevers. This topography was not necessary since the cantilevers have two additional topography sensing mechanisms. However, the obtained four topographic images could be used to compare the tip shape of each cantilever. The second and third rows of the images show results from the filtered piezoresistive reading and the unfiltered thermal reading, respectively. The measured sensitivities for the piezoresistive reading ranged from $(1.50 \pm 0.04) \times 10^{-7}$ to $(1.61 \pm 0.05) \times 10^{-7}$ V/V-nm and the sensitivities for the thermal reading ranged from $(4.80 \pm 0.06) \times 10^{-6}$ to $(6.00 \pm 0.09) \times 10^{-6}$ V/V-nm.

Most of the tests on the calibration grating except for the topography relying on the optical readout contained significant noise in their images. The major sources were 60 Hz and its integer multiples from the power electronics and laboratory environment. More efforts should follow to suppress them. Moreover, both the piezoresistive reading and the thermal reading were performed without any feedback control so that their signal readouts possibly contained abnormal spikes when the cantilever encountered a sudden change in local topography. Since both the piezoresistive reading and the thermal reading can be used for a feedback loop, it is recommended to construct a feedback control to eliminate the parasitic spikes and also prevent mechanical wear problems of the probe tip.

IV. SUMMARY AND CONCLUSION

This paper describes the design, fabrication and characterization of improved all-silicon microcantilever heaters with integrated piezoresistors. Instead of using metal traces, only doped silicon was used to suppress parasitic bending and prevent electromigration upon heating. Electrical and thermal crosstalks between the heater and the piezoresistor were thoroughly investigated and sensitivity comparison for the two topographic sensors embedded in a single

cantilever was demonstrated for the first time. The fabricated microcantilevers exhibited successful integration of a resistive heater with a piezoresistive element in each cantilever and four cantilevers were arrayed for parallel operations. In addition to individual cantilever characterization, array characterization was also performed on a calibration grating. The fabricated microcantilever array will be applicable to parallel scanning probe lithography and force spectroscopy. A compact customized AFM system could be constructed with either the heater or the piezoresistor. The results obtained in this paper will give guidelines for the fabrication and integration of large 1D or 2D arrays of multifunctional microcantilevers.

REFERENCES

[1] T. R. Albrecht and C. F. Quate, "Atomic resolution imaging of a nonconductor by atomic force microscopy," *J. Appl. Phys.*, vol. 62, pp. 2599-2602, 1987.

[2] N. V. Lavrik and P. G. Datskos, "Femtogram mass detection using photothermally actuated nanomechanical resonators," *Appl. Phys. Lett.*, vol. 82, pp. 2697-2699, 2003.

[3] M. Lutwyche, C. Andreoli, G. Binnig, J. Brugger, U. Drechsler, W. Häberle, H. Rohrer, H. Rothuizen, P. Vettiger, G. Yaralioglu, and C. Quate, "5 × 5 2D AFM cantilever arrays a first step towards a Terabit storage device," *Sens. Actuators A*, vol. 73, pp. 89-94, 1999.

[4] P. Vettiger, J. Brugger, M. Despont, U. Drechsler, U. Dürig, W. Häberle, M. Lutwyche, H. Rothuizen, R. Stutz, R. Widmer, and G. Binnig, "Ultrahigh density, high-data-rate NEMS-based AFM data storage system," *Microelectron. Eng.*, vol. 46, pp. 11-17, 1999.

[5] M. Despont, J. Brugger, U. Drechsler, U. Dürig, W. Häberle, M. Lutwyche, H. Rothuizen, R. Stutz, R. Widmer, G. Binnig, H. Rohrer, and P. Vettiger, "VLSI-NEMS chip for parallel AFM data storage," *Sens. Actuators A*, vol. 80, pp. 100-107, 2000.

[6] U. Dürig, G. Cross, M. Despont, U. Drechsler, W. Häberle, M. I. Lutwyche, H. Rothuizen, R. Stutz, R. Widmer, P. Vettiger, G. K. Binnig, W. P. King, and K. E. Goodson, ""Millipede" - an AFM data storage system at the frontier of nanotribology," *Tribol. Lett.*, vol. 9, pp. 25-32, 2000.

[7] P. Vettiger, G. Cross, M. Despont, U. Drechsler, U. Dürig, B. Gotsmann, W. Häberle, M. Lantz, H. Rothuizen, R. Stutz, and G. Binnig, "The "Millipede"-nanotechnology entering data storage," *IEEE Trans. Nanotechnol.*, vol. 1, pp. 39-64, 2002.

[8] S. C. Minne, S. R. Manalis, A. Atalar, and C. F. Quate, "Independent parallel lithography using the atomic force microscope," *J. Vac. Sci. Technol. B*, vol. 14, pp. 2456-2461, 1996.

[9] X. Wang and C. Liu, "Multifunctional probe array for nano patterning and imaging," *Nano Lett.*, vol. 5, pp. 1867-1872, 2005.

[10] S. C. Minne, G. Yaralioglu, S. R. Manalis, J. D. Adams, J. Zesch, A. Atalar, and C. F. Quate, "Automated parallel high-speed atomic force microscopy," *Appl. Phys. Lett.*, vol. 72, pp. 2340-2342, 1998.

[11] L. Aeschimann, A. Meister, T. Akiyama, B. W. Chui, P. Niedermann, H. Heinzelmann, N. F. De Rooij, U. Staufer, and P. Vettiger, "Scanning probe arrays for life sciences and nanobiology applications," *Microelectron. Eng.*, vol. 83, pp. 1698-1701, 2006.

[12] M. Despont, T. Altebaeumer, P. Bächtold, G. K. Binnig, G. Cherubini, U. Drechsler, U. Dürig, E. Eleftheriou, B. Gotsmann, W. Häberle, C. Hableitner, D. Jubin, A. Knoll, M. A. Lantz, A. Pantazi, H. Pozidis, H. Rothuizen, A. Sebastian, R. Stutz, P. Vettiger, D. Wiesmann, and J. Windeln, "A highly parallel probe-based storage system," *Digest of Papers - Microprocess and Nanotechnology 2004*, pp. 4-5, 2004.

[13] M. Despont, U. Drechsler, R. Yu, H. B. Pogge, and P. Vettiger, "Wafer-scale microdevice transfer/interconnect: Its application in an AFM-based data-storage system," *J. Microelectromech Syst.*, vol. 13, pp. 895-901, 2004.

[14] Y. S. Kim, C. S. Lee, W. H. Jin, S. Jang, H. J. Nam, and J. U. Bu, "100 × 100 thermo-piezoelectric cantilever array for SPM nano-data-storage application," *Sens. Materials*, vol. 17, pp. 57-63, 2005.

[15] K. Salaita, Y. H. Wang, J. Fragala, R. A. Vega, C. Liu, and C. A. Mirkin, "Massively parallel dip-pen nanolithography with 55000-pen two-dimensional arrays," *Angew. Chem. Int. Ed.*, vol. 45, pp. 7220-7223, 2006.

[16] J. Fritz, M. K. Baller, H. P. Lang, H. Rothuizen, P. Vettiger, E. Meyer, H. J. Güntherodt, C. Gerber, and J. K. Gimzewski, "Translating biomolecular recognition into nanomechanics," *Science*, vol. 288, pp. 316-318, 2000.

[17] M. K. Baller, H. P. Lang, J. Fritz, C. Gerber, J. K. Gimzewski, U. Drechsler, H. Rothuizen, M. Despont, P. Vettiger, F. M. Battiston, J. P. Ramseyer, P. Fornaro, E. Meyer, and H. J. Güntherodt, "A cantilever array-based artificial nose," *Ultramicroscopy*, vol. 82, pp. 1-9, 2000.

[18] F. M. Battiston, J. P. Ramseyer, H. P. Lang, M. K. Baller, C. Gerber, J. K. Gimzewski, E. Meyer, and H. J. Güntherodt, "A chemical sensor based on a microfabricated cantilever array with simultaneous resonance-frequency and bending readout," *Sens. Actuators B*, vol. 77, pp. 122-131, 2001.

[19] G. H. Wu, R. H. Datar, K. M. Hansen, T. Thundat, R. J. Cote, and A. Majumdar, "Bioassay of prostate-specific antigen (PSA) using microcantilevers," *Nature Biotechnol.*, vol. 19, pp. 856-860, 2001.

[20] Y. Arntz, J. D. Seelig, H. P. Lang, J. Zhang, P. Hunziker, J. P. Ramseyer, E. Meyer, M. Hegner, and C. Gerber, "Label-free protein assay based on a nanomechanical cantilever array," *Nanotechnol.*, vol. 14, pp. 86-90, 2003.

[21] F. Huber, M. Hegner, C. Gerber, H. J. Güntherodt, and H. P. Lang, "Label free analysis of transcription factors using microcantilever arrays," *Biosen. Bioelectronics*, vol. 21, pp. 1599-1605, 2006.

[22] S. L. Biswal, D. Raorane, A. Chaiken, and A. Majumdar, "Using a microcantilever array for detecting phase transitions and stability of DNA," *J. Assoc. Lab. Auto.*, vol. 11, pp. 222-226, 2006.

[23] Z. X. Yang, Y. Yu, X. X. Li, and H. F. Bao, "Nano-mechanical electro-thermal probe array used for high-density storage based on NEMS technology," *Microelec. Reliability*, vol. 46, pp. 805-810, 2006.

[24] S. A. Miller, K. L. Turner, and N. C. MacDonald, "Microelectromechanical scanning probe instruments for array architectures," *Rev. Sci. Instrum.*, vol. 68, pp. 4155-4162, 1997.

[25] M. Tortonese, R. C. Barrett, and C. F. Quate, "Atomic resolution with an atomic force microscope using piezoresistive detection," *Appl. Phys. Lett.*, vol. 62, pp. 834-836, 1993.

[26] G. Binnig, M. Despont, U. Drechsler, W. Häberle, M. Lutwyche, P. Vettiger, H. J. Mamin, B. W. Chui, and T. W. Kenny, "Ultrahigh-density atomic force microscopy data storage with erase capability," *Appl. Phys. Lett.*, vol. 74, pp. 1329-1331, 1999.

[27] W. P. King, T. W. Kenny, and K. E. Goodson, "Comparison of thermal and piezoresistive sensing approaches for atomic force microscopy topography measurements," *Appl. Phys. Lett.*, vol. 85, pp. 2086-2088, 2004.

[28] W. P. King, "Design analysis of heated atomic force microscope cantilevers for nanotopography measurements," *J. Micromech. Microeng.*, vol. 15, pp. 2441-2448, 2005.

[29] U. Dürig, "Fundamentals of micromechanical thermoelectric sensors," *J. Appl. Phys.*, vol. 98, p. 044906, 2005.

[30] M. A. Lantz, G. K. Binnig, M. Despont, and U. Drechsler, "A micromechanical thermal displacement sensor with nanometre resolution," *Nanotechnol.*, vol. 16, pp. 1089-1094, 2005.

[31] K. J. Kim, K. Park, J. Lee, Z. M. Zhang, and W. P. King, "Nanotopograpical imaging using a heated atomic froce microscope cantilever probe," *Sens. Actuators A*, vol. 136, pp. 95-103, 2007.

[32] K. Park, J. Lee, Z. M. Zhang, and W. P. King, "Nanotopograpical imaging with a heated atomic force microscope cantilever in tapping mode," *Rev. Sci. Instrum.*, vol. 78, p. 043709, 2007.

[33] Z. X. Yang, X. X. Li, Y. L. Wang, H. F. Bao, and M. Liu, "Micro cantilever probe array integrated with Piezoresistive sensor," *Microelec. J.*, vol. 35, pp. 479-483, 2004.

[34] N. Abedinov, P. Grabiec, T. Gotszalk, T. Ivanov, J. Voigt, and I. W. Rangelow, "Micromachined piezoresistive cantilever array with integrated resistive microheater for calorimetry and mass detection," *J. Vac. Sci. Technol. A*, vol. 19, pp. 2884-2888, 2001.

[35] B. A. Nelson, W. P. King, A. Laracuente, P. E. Sheehan, and L. J. Whitman, "Direct deposition of continuous metal nanostructures by thermal dip-pen nanolithography," *Appl. Phys. Lett.*, vol. 88, p. 033104, 2006.

[36] B. Gotsmann, U. Dürig, J. Frommer, and C. J. Hawker, "Exploiting chemical switching in a Diels-Alder polymer for nanoscale probe lithography and data storage," *Adv. Func. Mat.*, vol. 16, pp. 1499-1505, 2006.

[37] E. O. Sunden, T. L. Wright, J. Lee, S. A. Graham, and W. P. King, "Room temperature chemical vapor deposition and mass detection on a heated atomic force microscope cantilever," *Appl. Phys. Lett.*, vol. 88, p. 033107, 2006.

[38] R. Szoszkiewicz, T. Okada, S. C. Jones, T. D. Li, W. P. King, S. R. Marder, and E. Riedo, "High-speed, sub-15 nm feature size thermochemical nanolithography," *Nano Lett.*, vol. 7, pp. 1064-1069, 2007.

[39] T. Arai and M. Tomitori, "Removal of contamination and oxide layers from UHV-AFM tips," *Appl. Phys. A*, vol. 66, pp. S319-S323, 1998.

[40] M. Tomitori and T. Arai, "Tip cleaning and sharpening processes for noncontact atomic force microscope in ultrahigh vacuum," *Appl. Surf. Sci.*, vol. 140, pp. 432-438, 1999.

[41] S. L. Biswal, D. Raorane, A. Chaiken, H. Birecki, and A. Majumdar, "Nanomechanical detection of DNA melting on microcantilever surfaces," *Anal. Chem.*, vol. 78, pp. 7104-7109, 2006.

[42] J. Lee, T. Beechem, T. L. Wright, B. A. Nelson, S. Graham, and W. P. King, "Electrical, thermal, and mechanical characterization of silicon microcantilever heaters," *J. Microelectromech Syst.*, vol. 15, pp. 1644-1655, 2006.

[43] J. R. Black, "Electromigration-A brief survey and some recent results," *IEEE Trans. Electron. Devices*, vol. 16, pp. 338-347, 1969.

[44] C. Liu, *Foundations of MEMS,* Upper Saddle River, NJ: Pearson/Prentice Hall, 2006.

[45] X. Yu, D. Zhang, W. Wang, and T. Li, "A sensor platform based on piezoresistive cantilever," presented at Electron Devices and Solid-State Circuits, 2003 IEEE Conference on, 2003.

[46] J. A. Harley and T. W. Kenny, "1/F noise considerations for the design and process optimization of piezoresistive cantilevers," *J. Microelectromech Syst.*, vol. 9, pp. 226-235, 2000.

[47] T. L. Wright, "Design and fabrication of heated atomic force microscope cantilevers," M. S. Thesis, Woodruff school of Mech. Eng., Georgia Inst. of Tech., Atlanta, GA, 2005.

[48] B. W. Chui, T. W. Kenny, H. J. Mamin, B. D. Terris, and D. Rugar, "Independent detection of vertical and lateral forces with a sidewall-implanted dual-axis piezoresistive cantilever," *Appl. Phys. Lett.*, vol. 72, pp. 1388-1390, 1998.

[49] X. M. Yu, J. Thaysen, O. Hansen, and A. Boisen, "Optimization of sensitivity and noise in piezoresistive cantilevers," *J. Appl. Phys.*, vol. 92, pp. 6296-6301, 2002.

[50] S. Reggiani, M. Valdinoci, L. Colalongo, M. Rudan, G. Baccarani, A. D. Stricker, F. Illien, N. Felber, W. Fichtner, and L. Zullino, "Electron and hole mobility in silicon at large operating temperatures - Part I: Bulk mobility," *IEEE Trans. Electron. Devices*, vol. 49, pp. 490-499, 2002.

[51] S. D. Senturia, *Microsystem Design,* Boston: Kluwer Academic Publishers, 2001.

[52] B. W. Chui, T. D. Stowe, Y. S. Ju, K. E. Goodson, T. W. Kenny, H. J. Mamin, B. D. Terris, and R. P. Ried, "Low-stiffness silicon cantilever with integrated heaters and piezoresistive sensors for high-density data storage," *J. Microelectromech Syst.*, vol. 7, pp. 69-78, 1998.

[53] B. W. Chui, M. Asheghi, Y. S. Ju, K. E. Goodson, T. W. Kenny, and H. J. Mamin, "Intrinsic-carrier thermal runaway in silicon microcantilevers," *Microscale Thermophys. Eng.*, vol. 3, pp. 217-228, 1999.

[54] M. Kuball, J. M. Hayes, M. J. Uren, T. Martin, J. C. H. Birbeck, R. S. Balmer, and B. T. Hughes, "Measurement of temperature in active high-power AlGaN/GaN HFETs using Raman spectroscopy," *IEEE Elec. Dev. Lett.*, vol. 23, pp. 7-9, 2002.

[55] M. Kuball, S. Rajasingam, A. Sarua, M. J. Uren, T. Martin, B. T. Hughes, K. P. Hilton, and R. S. Balmer, "Measurement of temperature distribution in multifinger AlGaN/GaN heterostructure field-effect transistors using micro-Raman spectroscopy," *Appl. Phys. Lett.*, vol. 82, pp. 124-126, 2003.

[56] R. Diffenderfer, *Electronic devices : systems and applications,* Clifton Park, N.Y.: Thomson/Delmar Learning, 2005.

[57] J. Lee and W. P. King, "Microcantilever hotplates: Design, fabrication, and characterization," *Sens. Actuators A*, vol. 136, pp. 291-298, 2007.

[58] B. W. Chui, L. Aeschimann, T. Akiyama, U. Staufer, N. F. d. Rooij, J. Lee, F. Goericke, W. P. King, and P. Vettiger, "Advanced temperature compensation for piezoresistive cantilevers using 45-degree angle resistor pairs," *Rev. Sci. Instrum.*, vol. 78, p. 043706, 2007.

[59] R. Hull and INSPEC (Information service), *Properties of crystalline silicon,* London: INSPEC, 1999.

[60] J. Lee, T. L. Wright, M. R. Abel, E. O. Sunden, A. Marchenkov, S. Graham, and W. P. King, "Thermal conduction from microcantilever heaters in partial vacuum," *J. Appl. Phys.*, vol. 101, p. 014906 , 2007.

LIST OF TABLES

Table I. Summarized basic characterization results.

	Heater	Piezoresistor
Measured electrical resistance ($k\Omega$)	0.466 ± 0.005	7.65 ± 0.04
Simulated electrical resistance ($k\Omega$)	0.57	8.60
TCR (Ω/Ω-°C)	$(2.01 \pm 0.04) \times 10^{-3}$	$(8.3 \pm 0.4) \times 10^{-4}$
Deflection sensitivity (V/V-μm)	$(7.9 \pm 0.5) \times 10^{-5}$	$(4.25 \pm 0.05) \times 10^{-4}$
Spring constant (N/m)	2.3 ± 0.2	
Resonance frequency (kHz)	73.0 ± 0.7	
Quality factor	118 ± 9	

Table II. Sensitivity, noise, and resolution of the heater and the piezoresistor during independent operation.

		3 V	4 V	5 V	6 V
Heater	Sensitivity ($\mu V/nm$)	3.0 ± 0.2	8.4 ± 0.2	18.5 ± 0.2	35.4 ± 0.2
	Noise ($\mu V/\sqrt{Hz}$)	1.39 ± 0.07	1.64 ± 0.08	1.80 ± 0.09	2.1 ± 0.1
	Resolution ($nm/\sqrt{Hz}$)	0.46 ± 0.03	0.19 ± 0.01	0.097 ± 0.005	0.058 ± 0.003
Piezoresistor	Sensitivity ($\mu V/nm$)	0.77 ± 0.02	1.09 ± 0.02	1.25 ± 0.03	1.50 ± 0.02
	Noise ($\mu V/\sqrt{Hz}$)	2.7 ± 0.3	2.7 ± 0.3	3.0 ± 0.3	3.0 ± 0.3
	Resolution ($nm/\sqrt{Hz}$)	3.4 ± 0.4	2.5 ± 0.3	2.4 ± 0.2	2.0 ± 0.2

LIST OF FIGURES WITH CAPTIONS

Fig. 1. (a) Single cantilever showing different doping regions for the heater, legs, and the piezoresistor. (b) Design of 1 × 4 array of microcantilever heaters with integrated piezoresistors and dimensions for an individual cantilever in μm.

Fig. 2. (a) Simulated doping concentration of low-doped phosphorus, high-doped phosphorus, and medium-doped boron after implantation and post diffusion. (b) Resistivity after implantation and post diffusion. *P* and *B* indicate phosphorus and boron, respectively, and subscripts *H*, *M*, and *L* denote high, intermediate, and low doping, respectively.

Fig. 3. Seven major fabrication steps to make the microcantilever heater array.

Fig. 4. (a) (b) SEM images of the fabricated array chip. Inset in (a) shows the sharp tip near the low-doped resistive heater. (c) Custom PCB and flexible ribbon cable to mount an array chip and make electrical connections. Inset shows a wire-bonded array chip.

Fig. 5. (a) Electrical resistance and temperature of the heater as a function of power dissipation in the heater. (b) Electrical resistance and maximum temperature of the piezoresistor as a function of power dissipation in the piezoresistor. (c) Normalized resistance comparison between the heater and the piezoresistor. (d) Normalized resistance of the heater and the piezoresistor as a function of the maximum temperature in each resistor. Temperature data were obtained using Raman spectroscopy. These measurements are made on a free-standing cantilever far away from a substrate.

Fig. 6. Diode I-V characteristics of the *p-n* junction between one leg for the heater and one leg for the piezoresistor. The "on voltage" is around 0.6 V which is appropriate for silicon *p-n* diodes.

Fig. 7. IR micrographs with 5 mW power dissipation in the piezoresistor, 5 mW power dissipation in the heater, and 5 mW power dissipation in both the piezoresistor and the heater.

Fig. 8. Cantilever deflection sensitivity. (a) Bridge voltage output as a function of the tip deflection where bias voltage to the Wheatstone bridge is 2 V. Measurements are repeated with the heater powered. (b) Deflection sensitivity of the piezoresistors decreases as power dissipation in the heater increases. (c) Voltage offset linearly increases with power dissipation in the heater. (d) Voltage output from another bridge as a function of the tip deflection where bias voltage to the Wheatstone bridge is 2 V.

Fig. 9. Piezoresistive reading and thermal reading upon independent operation. Either the piezoresistor or the heater is operated independently. The left images show filtered piezoresistive reading with 20 dB gain and the right images show unfiltered thermal reading from a single cantilever. Bias Voltages to each Wheatstone bridge are 4 V (top) and 5 V (bottom).

Fig. 10. Piezoresistive reading and thermal reading upon combined operation. Both the piezoresistor and the heater are operated simultaneously. The left images show filtered piezoresistive reading with 20 dB gain and the right images show unfiltered thermal reading from a single cantilever. Bias Voltages to the two Wheatstone bridges are 4 V (top) and 5 V (bottom).

Fig. 11. Topography sensitivity comparison between piezoresistive reading and thermal reading for both independent and combined operation.

Fig. 12. (a) Optical lever topography, (b) Filtered piezoresistive reading with 20 dB gain, and (c) Unfiltered thermal reading. Images on each column are obtained from each cantilever in the given array. After obtaining optical lever topography, all four cantilevers are operated simultaneously but either the piezoresistor or the heater in a cantilever is operated at a time with 4 V bias voltage.

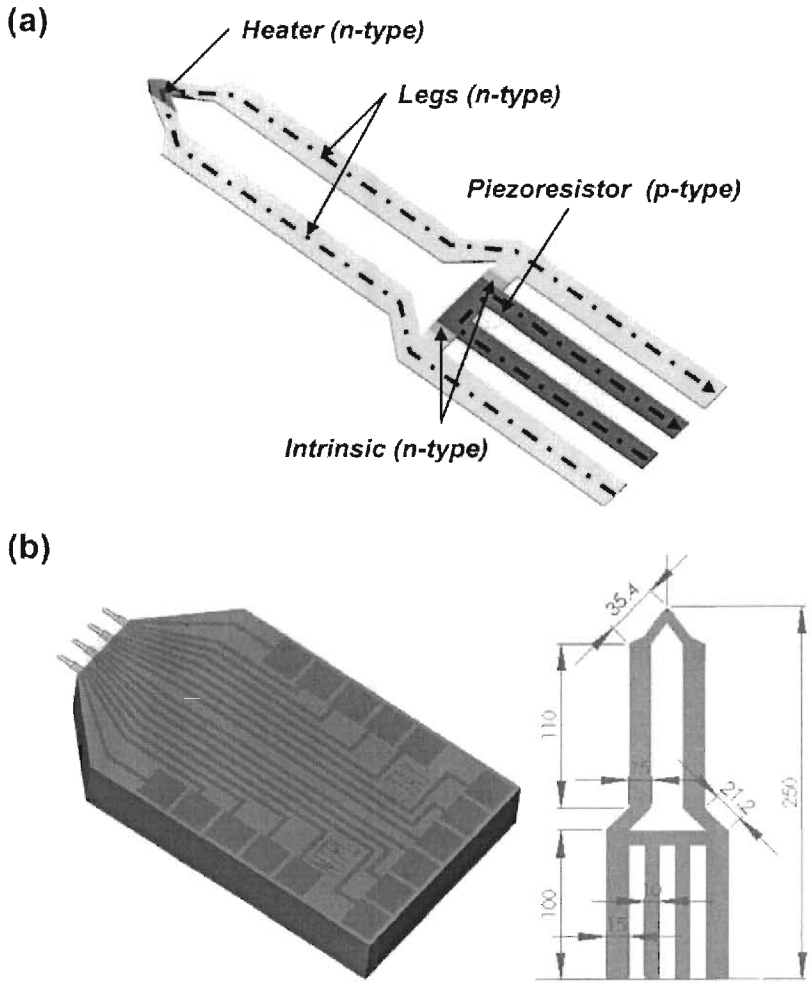
(a)
Heater (n-type)
Legs (n-type)
Piezoresistor (p-type)
Intrinsic (n-type)
(b)
35.4
110
212
250
100

Fig. 1.

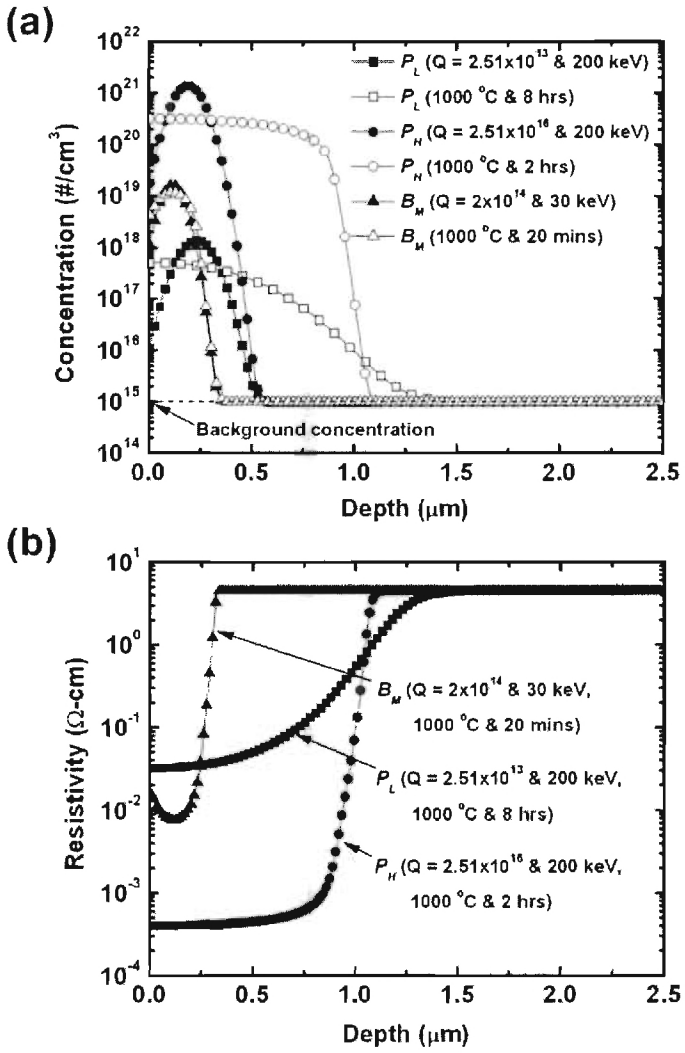
(a)
Concentration (#/cm^3)
P_L (Q = 2.51x10^{13} & 200 keV)
P_L (1000 °C & 8 hrs)
P_H (Q = 2.51x10^{16} & 200 keV)
P_H (1000 °C & 2 hrs)
B_M (Q = 2x10^{14} & 30 keV)
B_M (1000 °C & 20 mins)
Background concentration
Depth (μm)
(b)
Resistivity (Ω-cm)
B_M (Q = 2x10^{14} & 30 keV, 1000 °C & 20 mins)
P_L (Q = 2.51x10^{13} & 200 keV, 1000 °C & 8 hrs)
P_H (Q = 2.51x10^{16} & 200 keV, 1000 °C & 2 hrs)
Depth (μm)

Fig. 2.

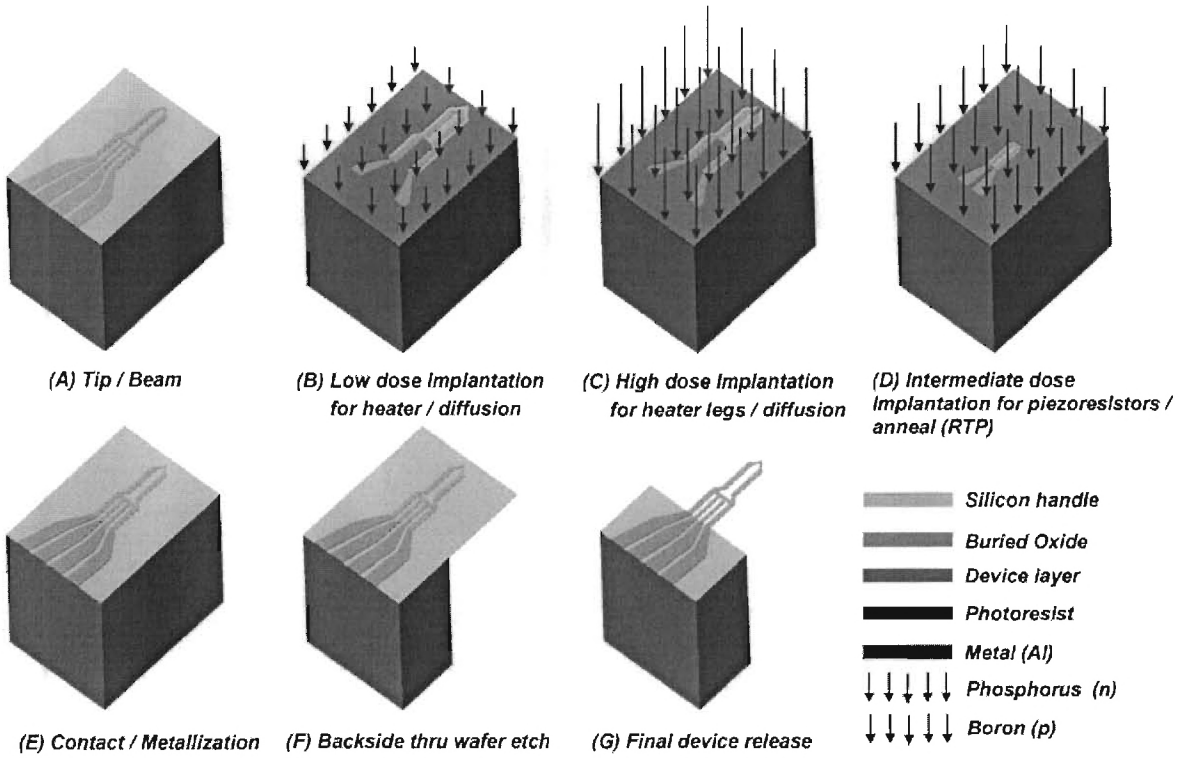
(A) Tip / Beam
(B) Low dose implantation for heater / diffusion
(C) High dose implantation for heater legs / diffusion
(D) Intermediate dose implantation for piezoresistors / anneal (RTP)
(E) Contact / Metallization
(F) Backside thru wafer etch
(G) Final device release
Silicon handle
Buried Oxide
Device layer
Photoresist
Metal (Al)
Phosphorus (n)
Boron (p)

Fig. 3.

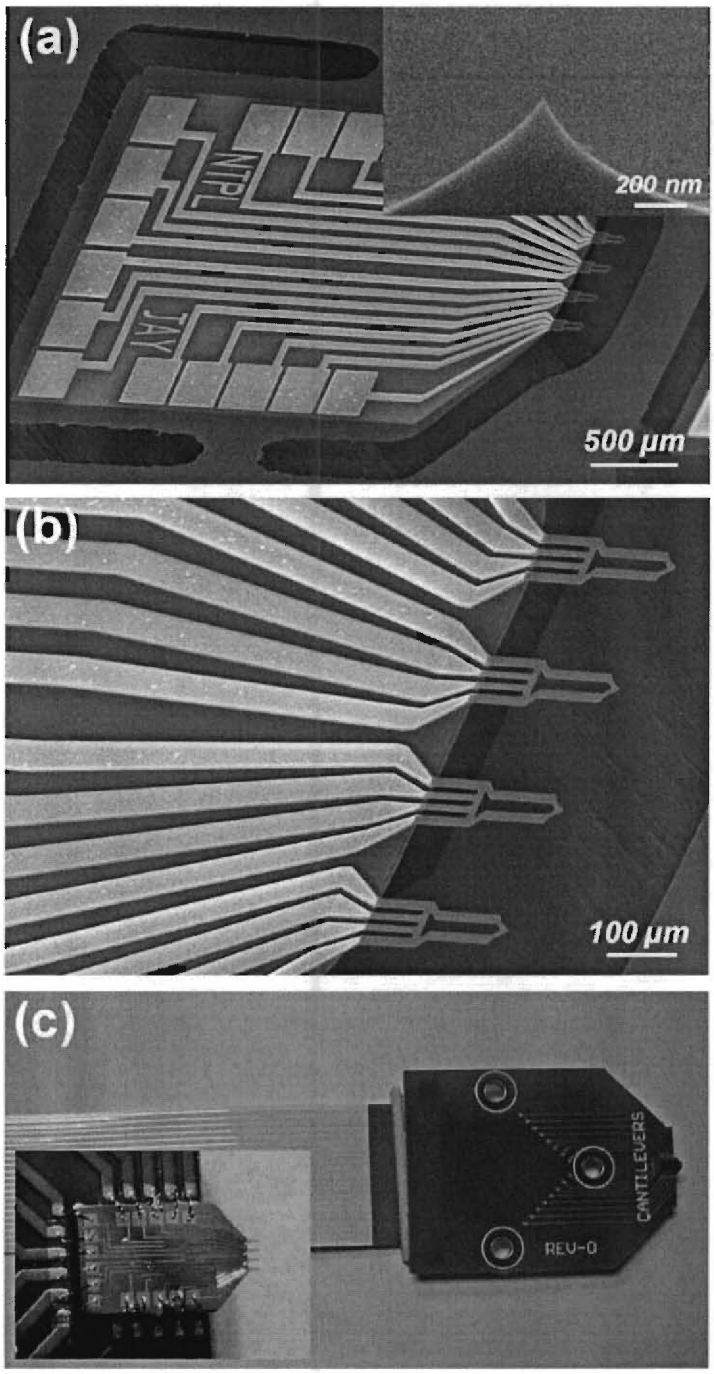

Fig. 4.

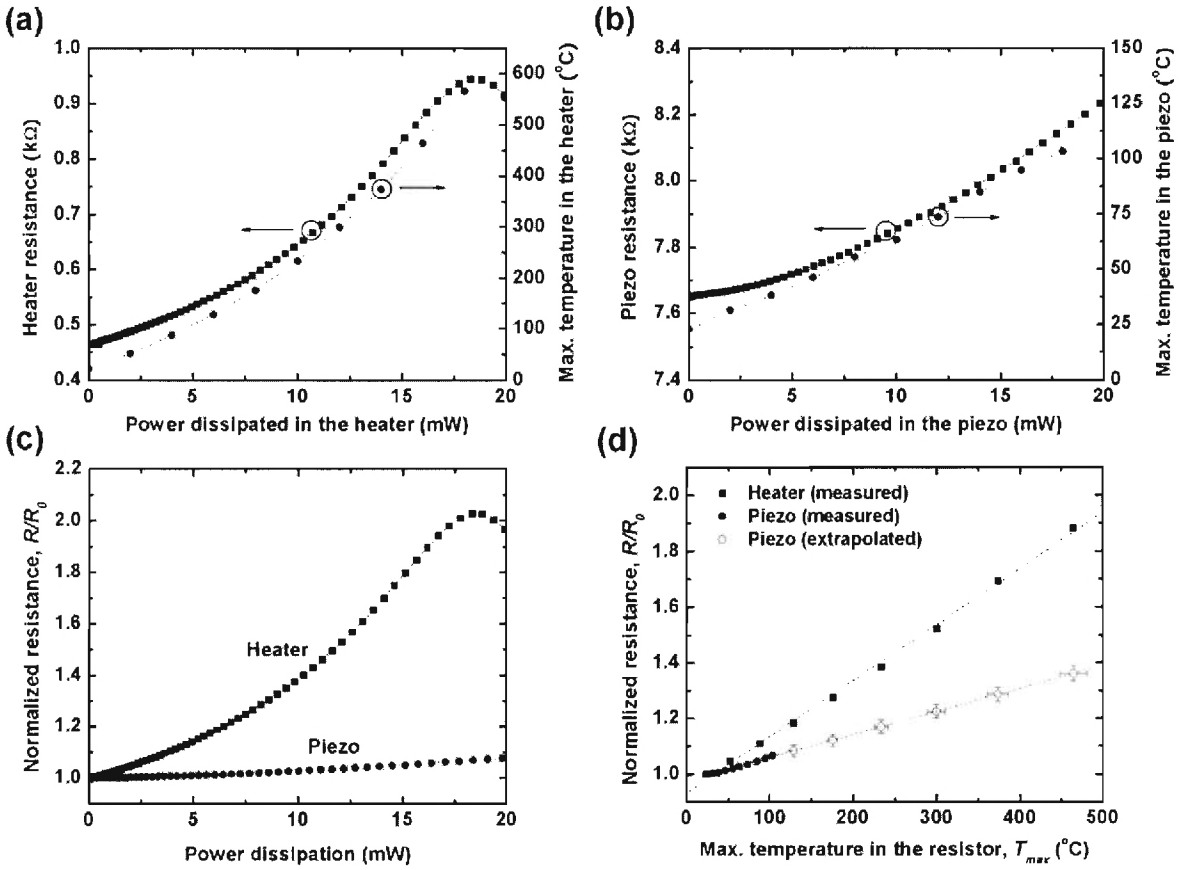
(a)
Heater resistance (kΩ)
Max. temperature in the heater (°C)
Power dissipated in the heater (mW)
(b)
Piezo resistance (kΩ)
Max. temperature in the piezo (°C)
Power dissipated in the piezo (mW)
(c)
Normalized resistance, R/R0
Heater
Piezo
Power dissipation (mW)
(d)
Normalized resistance, R/R0
Heater (measured)
Piezo (measured)
Piezo (extrapolated)
Max. temperature in the resistor, Tmax (°C)

Fig. 5.

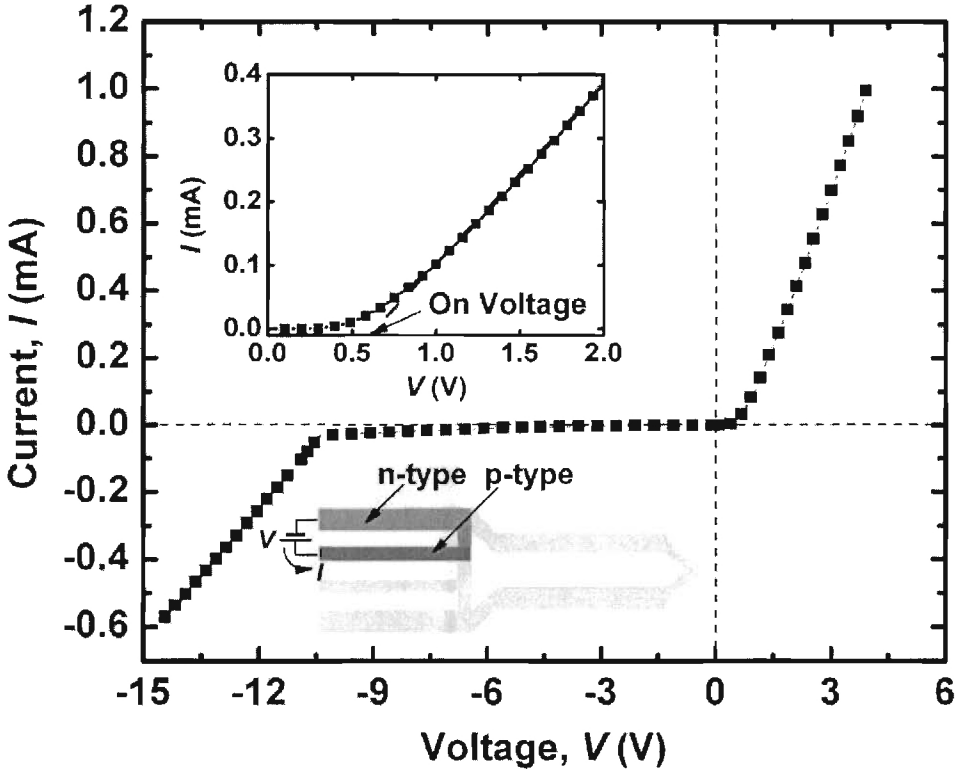

Fig. 6.

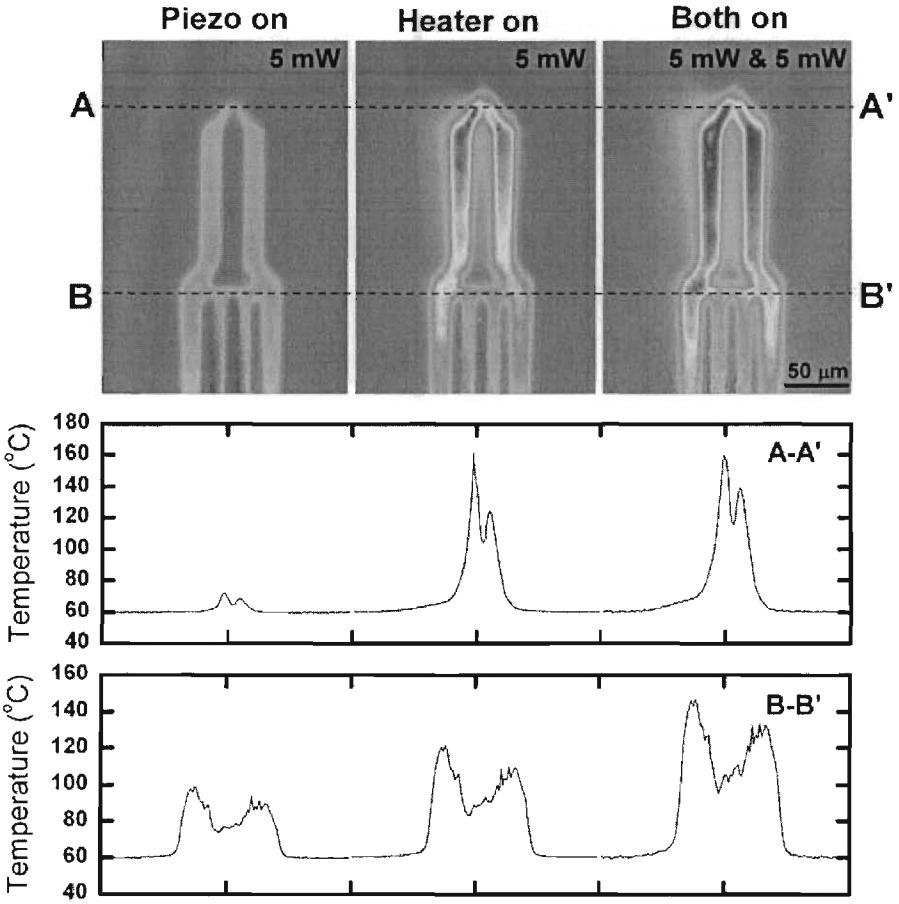
Piezo on
Heater on
Both on
5 mW
5 mW
5 mW & 5 mW
A
A'
B
B'
50 μm
Temperature (°C)
180
160
140
120
100
80
60
40
A-A'
Temperature (°C)
160
140
120
100
80
60
40
B-B'

Fig. 7.

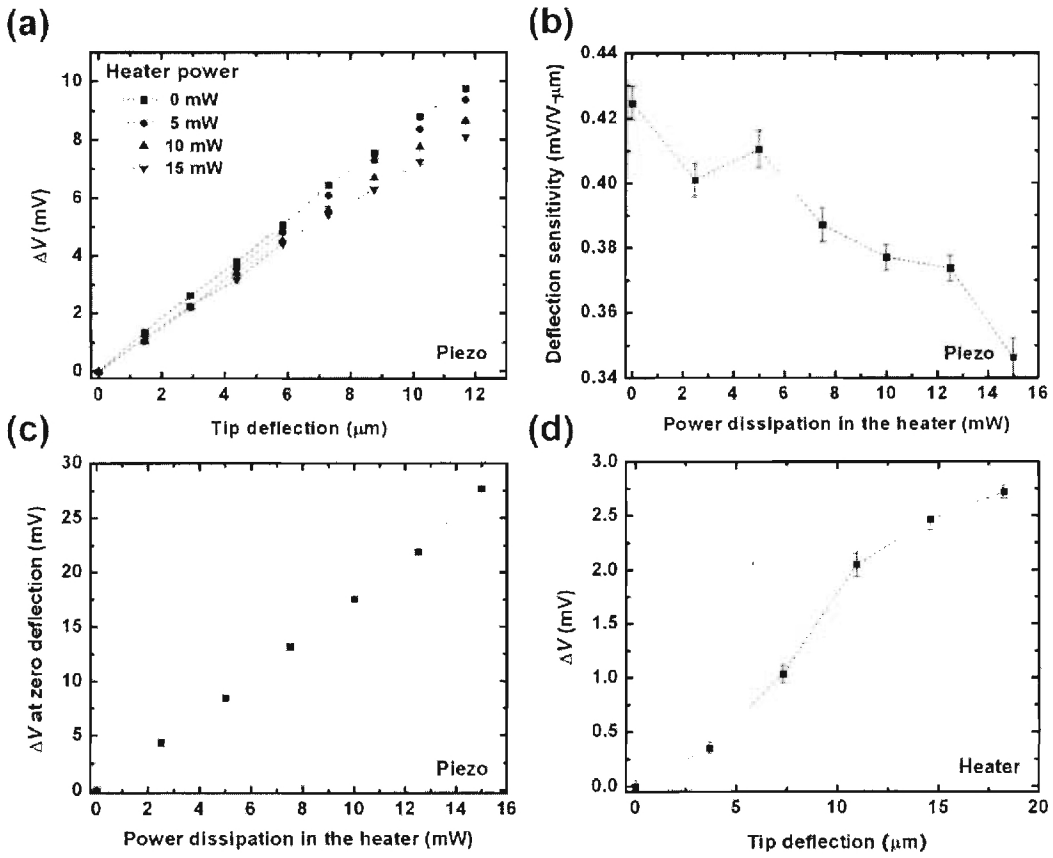
(a)
Heater power
0 mW
5 mW
10 mW
15 mW
ΔV (mV)
Tip deflection (μm)
Piezo
(b)
Deflection sensitivity (mV/V-μm)
Power dissipation in the heater (mW)
Piezo
(c)
ΔV at zero deflection (mV)
Power dissipation in the heater (mW)
Piezo
(d)
ΔV (mV)
Tip deflection (μm)
Heater

Fig. 8.

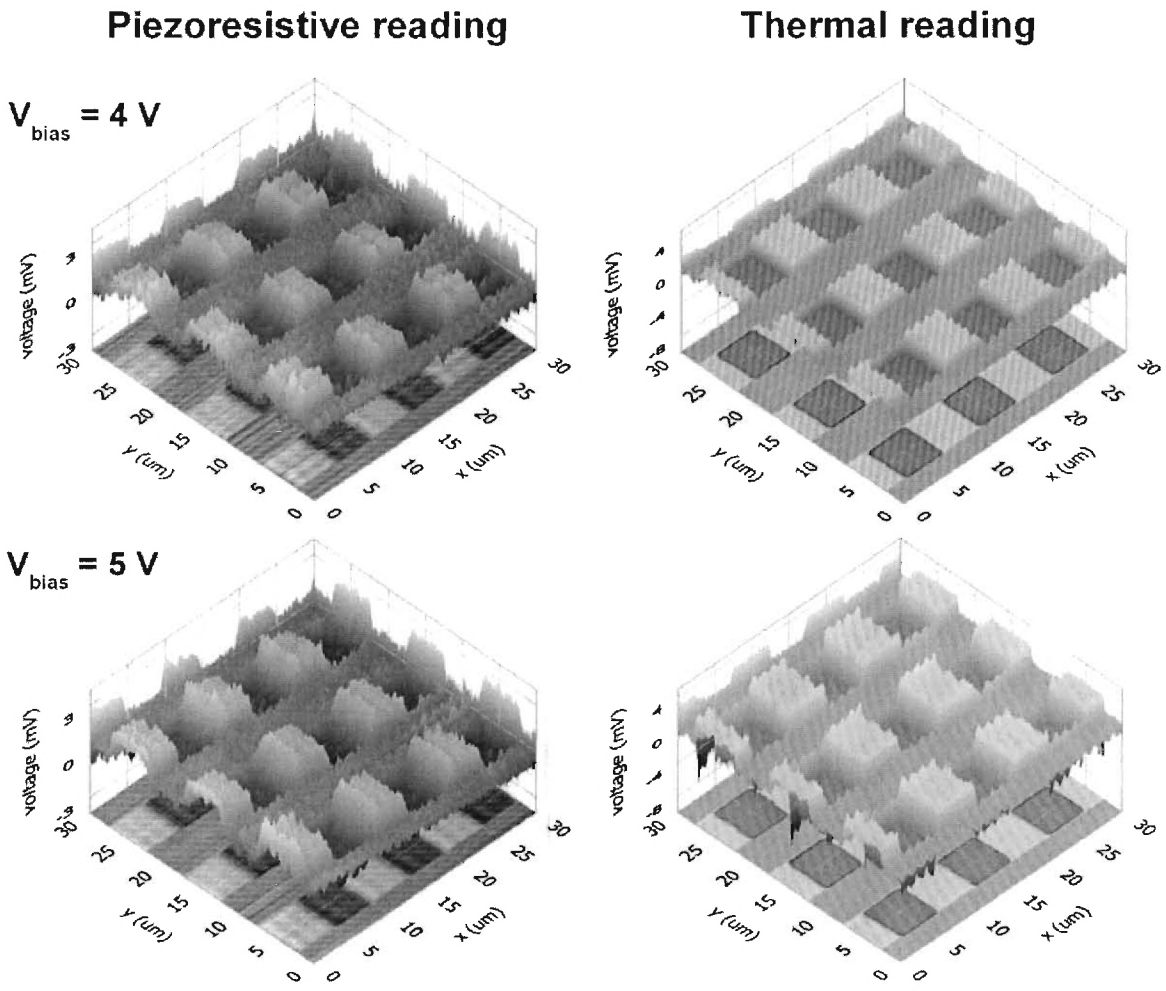
Piezoresistive reading
Thermal reading
V bias = 4 V
V bias = 5 V
voltage (mV)
y (um)
x (um)

Fig. 9.

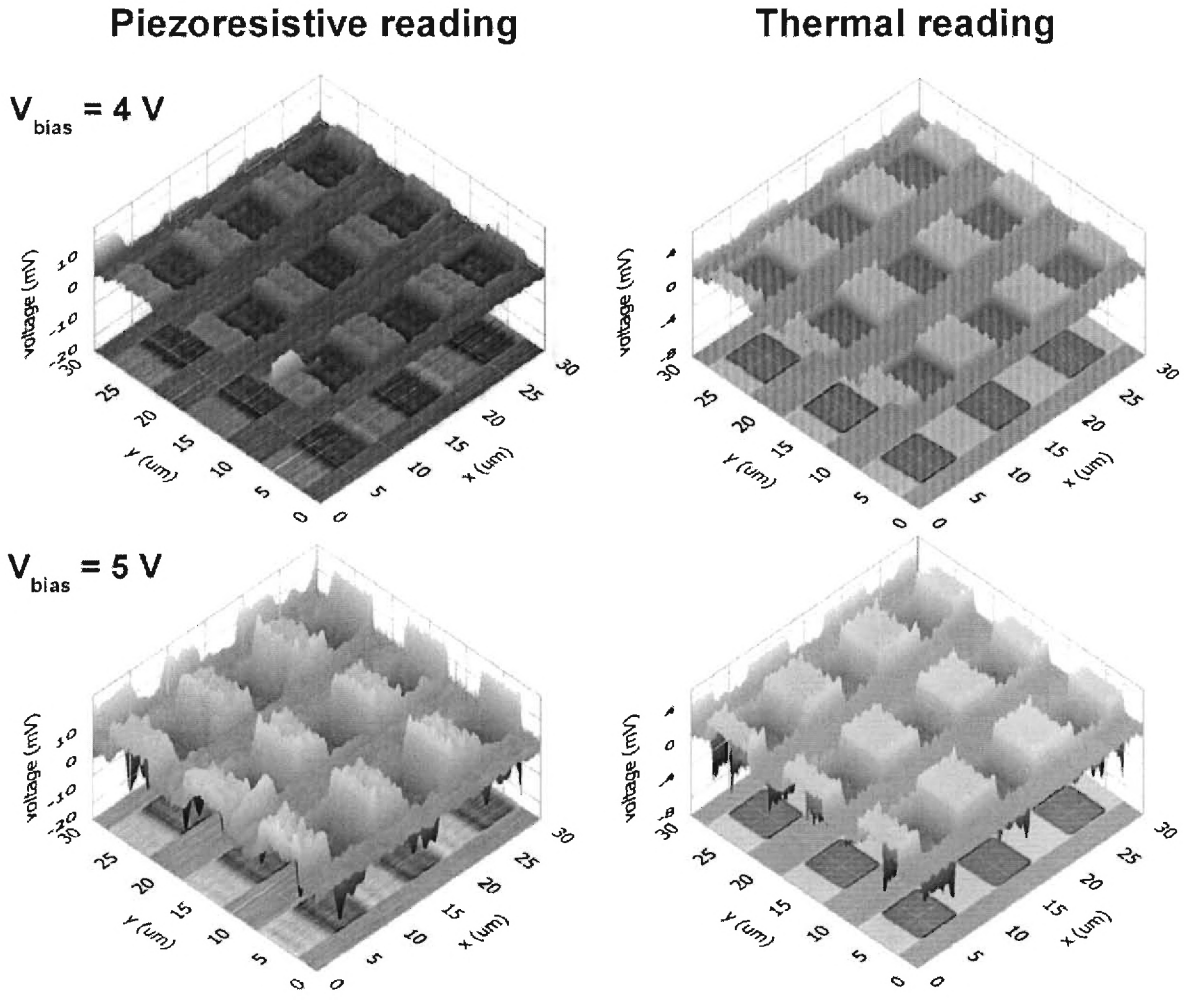
Piezoresistive reading
Thermal reading
V bias = 4 V
V bias = 5 V
voltage (mV)
y (um)
x (um)

Fig. 10.

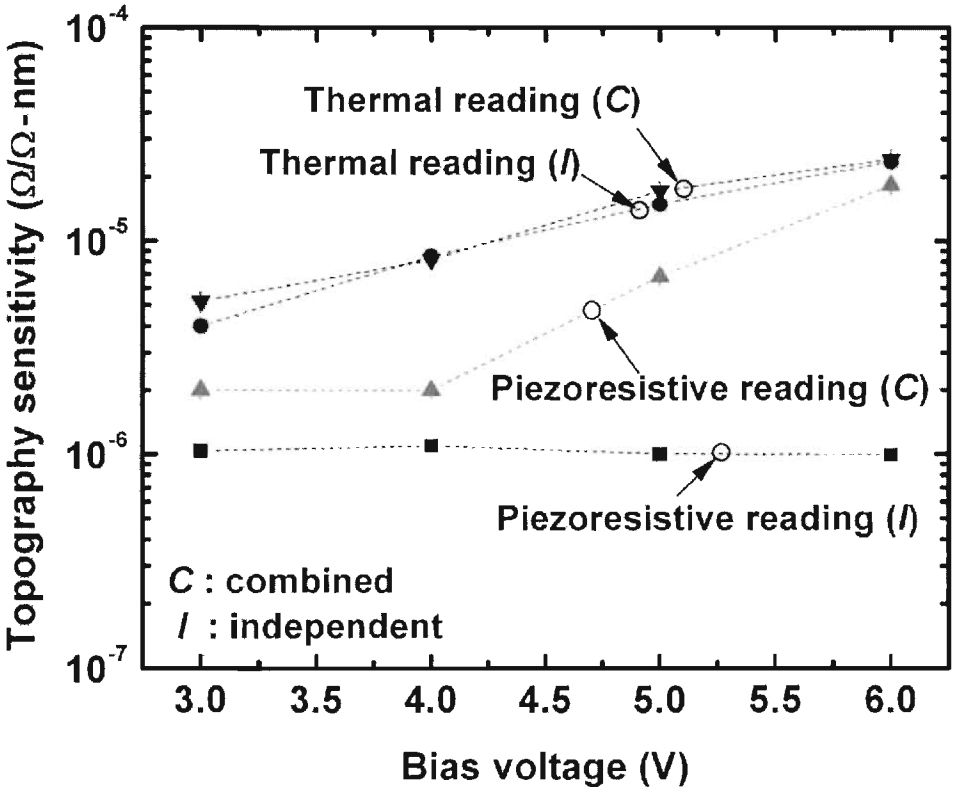
Topography sensitivity (Ω/Ω-nm)
10^-4
10^-5
10^-6
10^-7
Thermal reading (C)
Thermal reading (I)
Piezoresistive reading (C)
Piezoresistive reading (I)
C : combined
I : independent
3.0
3.5
4.0
4.5
5.0
5.5
6.0
Bias voltage (V)

Fig. 11.

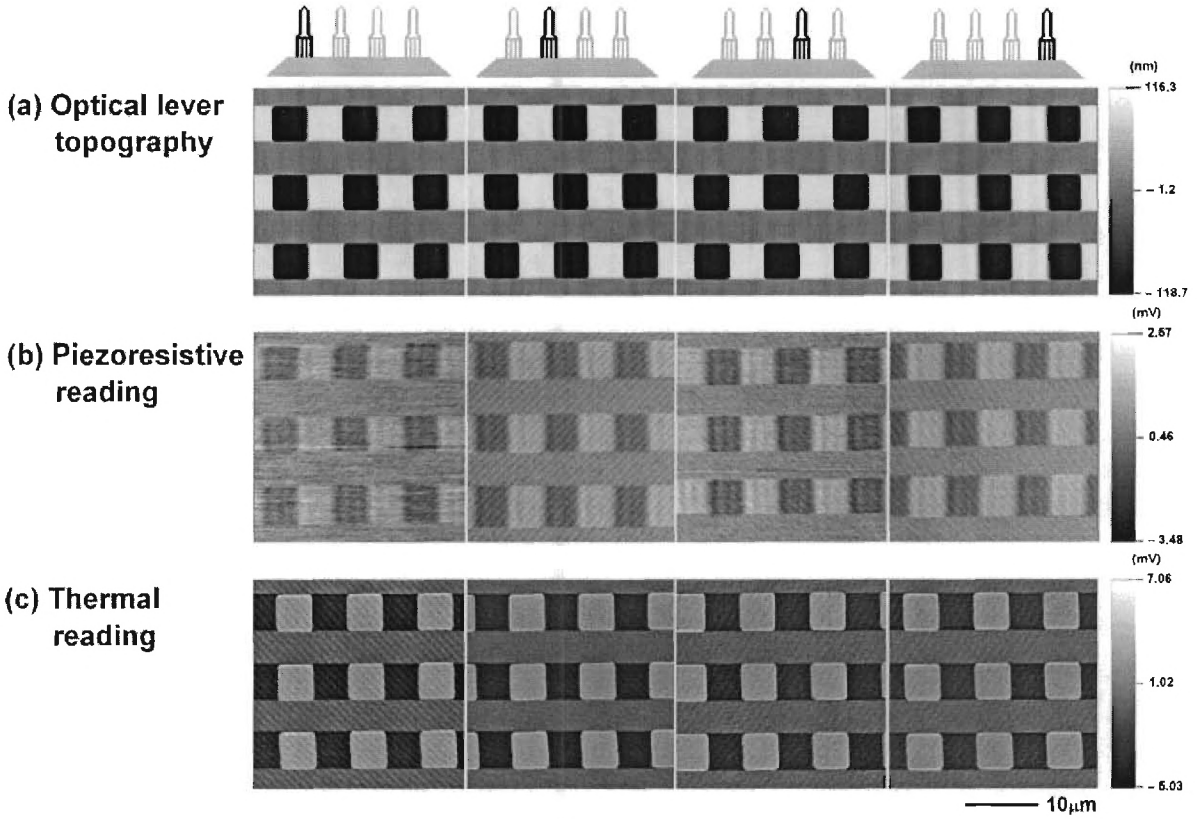
(a) Optical lever topography
(b) Piezoresistive reading
(c) Thermal reading
(nm)
116.3
1.2
118.7
(mV)
2.67
0.46
3.48
(mV)
7.06
1.02
5.03
10μm

Fig. 12.